Eur J Nucl Med Mol Imaging (2008) 35:1812–1823
DOI 10.1007/s00259-008-0756-7

ORIGINAL ARTICLE

Correction of oral contrast artifacts in CT-based attenuation correction of PET images using an automated segmentation algorithm

Alireza Ahmadian · Mohammad R. Ay · Javad H. Bidgoli · Saeed Sarkar · Habib Zaidi

Received: 31 December 2007 / Accepted: 19 February 2008 / Published online: 17 April 2008

Abstract
Purpose Oral contrast is usually administered in most X-ray computed tomography (CT) examinations of the abdomen and the pelvis as it allows more accurate identification of the bowel and facilitates the interpretation of abdominal and pelvic CT studies. However, the misclassification of contrast medium with high-density bone in CT-based attenuation correction (CTAC) is known to generate artifacts in the attenuation map (μmap), thus resulting in overcorrection for attenuation of positron emission tomography (PET) images. In this study, we developed an automated algorithm for segmentation and classification of regions containing oral contrast medium to correct for artifacts in CT-attenuation-corrected PET images using the segmented contrast correction (SCC) algorithm.
Methods The proposed algorithm consists of two steps: first, high CT number object segmentation using combined region- and boundary-based segmentation and second, object classification to bone and contrast agent using a knowledge-based nonlinear fuzzy classifier. Thereafter, the CT numbers of pixels belonging to the region classified as contrast medium are substituted with their equivalent effective bone CT numbers using the SCC algorithm. The generated CT images are then down-sampled followed by Gaussian smoothing to match the resolution of PET images. A piecewise calibration curve was then used to convert CT pixel values to linear attenuation coefficients at 511 keV.
Results The visual assessment of segmented regions performed by an experienced radiologist confirmed the accuracy of the segmentation and classification algorithms for delineation of contrast-enhanced regions in clinical CT images. The quantitative analysis of generated μmaps of 21 clinical CT colonoscopy datasets showed an overestimation ranging between 24.4% and 37.3% in the 3D-classified regions depending on their volume and the concentration of contrast medium. Two PET/CT studies known to be problematic demonstrated the applicability of the technique in clinical setting. More importantly, correction of oral contrast artifacts improved the readability and interpretation of the PET scan and showed substantial decrease of the SUV (104.3%) after correction.
Conclusions An automated segmentation algorithm for classification of irregular shapes of regions containing contrast medium was developed for wider applicability of the SCC algorithm for correction of oral contrast artifacts during the CTAC procedure. The algorithm is being refined and further validated in clinical setting.

Keywords PET · X-ray CT · Attenuation correction · Segmentation · Contrast medium

A. Ahmadian · M. R. Ay (✉) · J. H. Bidgoli · S. Sarkar
Research Center for Science and Technology in Medicine, Medical Sciences/University of Tehran, Tehran, Iran
e-mail: mohammadreza_ay@tums.ac.ir

A. Ahmadian · M. R. Ay · S. Sarkar
Department of Medical Physics and Biomedical Engineering, School of Medicine, Medical Sciences/University of Tehran, Tehran, Iran

J. H. Bidgoli
Department of Electrical and Computer Engineering, East Tehran Azad University, Tehran, Iran

H. Zaidi
Division of Nuclear Medicine, Geneva University Hospital, 1211 Geneva, Switzerland

Introduction

The marketplace is clearly showing that most operational standalone PET scanners are being replaced by modern high-end dual-modality positron emission tomography (PET)/CT systems. Combined PET/CT systems seem to offer many advantages over standalone PET, including decreased scanning time and increased accuracy in tumor localization [1]. Oral contrast medium is usually administered in most CT examinations of the abdomen or the pelvis as it allows more accurate identification of the bowel and facilitates the interpretation of abdominal and pelvic CT studies. Although there is a general consensus that the administration of oral contrast medium enhances the diagnostic value of CT in most examinations of the abdomen or the pelvis, its application on combined PET/CT systems is not yet fully established [2, 3]. More recently, Tateishi et al. [4] showed that contrast-enhanced PET/CT is more accurate than non-enhanced PET/CT in determining the regional nodal status of rectal cancer. Moreover, Mainenti et al. [5] reported that PET/CT colonography allows a correct characterization of all cases of colorectal focal radiotracer uptake.

The main challenge is the possibility of adverse effects on CT-based attenuation correction (CTAC) of PET data owing to the fact that misclassification of contrast medium with high-density bone is known to generate artifacts in the attenuation map (μmap). This results in overcorrection for photon attenuation, consequently overestimating the apparent reconstructed activity concentration of the radiotracer in the contrast-enhanced region. This is due to the high attenuation coefficient of contrast agent materials at the low effective energy of the polychromatic X-ray spectra, which results in high CT numbers in the region accumulating contrast agent and thus a correspondingly high attenuation coefficient at 511 keV through misclassification with high-density cortical bone [6, 7].

The issue of whether the use of oral contrast medium in dual-modality PET/CT scanning produces medically significant artifacts is still controversial with some studies corroborating [2, 8–11] and others contradicting [6, 7, 12, 13] the fact that the presence of contrast medium can be a source of errors and artifact when the CT data are used for attenuation correction of PET images. Notwithstanding, various strategies have been proposed for correction of contrast-induced artifacts in CTAC [14]. This includes the use of separate bi-linear calibration curves for conversion of CT numbers to linear attenuation coefficients at 511 keV for bone-soft tissue and contrast agent-soft tissue combinations [15], image segmentation followed by correct scaling of contrast-enhanced CT images [6, 16, 17], and dual-energy decomposition methods, which combine two CT scans from the same region at different X-ray energies to generate accurate attenuation coefficients at any desired photon energy [18]. An alternative is the acquisition of both pre- and post-contrast CT scans to minimize possible artifacts contributed by the presence of contrast media [1].

The correction algorithm used in this work is based on the segmented contrast correction (SCC) method [6]. Although the efficiency of the SCC technique has been demonstrated using both phantom and clinical studies and proved to accurately recover lesion size and uptake [6, 7], its applicability is still limited to simple geometrical shapes, reflecting the spatial distribution of contrast medium owing to the limitations of currently available segmentation algorithms. This limitation renders the algorithm useless in clinical area where irregular shapes of regions containing contrast medium are typically found in clinical studies. The main problem for the clinical application of the SCC algorithm is the difficulty encountered in the segmentation and classification of contrast-enhanced fluids (CEF) from patient's CT images. Automated segmentation of bone and CEF from CT images is not an easy task. Bones come in a variety of shapes and have complex internal and external structures with similar or higher CT values than other biological tissues. More specifically, cortical bone is dense and its attenuation coefficients, expressed in Hounsfield units (HU), are rather constant across individuals, whereas trabecular bone is spongy with hard and dense outer surface layer and marrow having density slightly above that of soft tissue [19]. This complexity makes bone segmentation tricky in particular in the presence of CEF whose density range overlaps with the density range of bone. In addition, CEF have irregular shape and size and can have different attenuation properties depending on their type, density, and diet. Therefore, the classification of regions containing bone and contrast medium in contrast-enhanced CT images is a challenging task given the similarity of CT numbers in these regions in the majority of clinical situations. Consequently, segmentation using simple intensity thresholding will not work in these situations [20–22].

Other segmentation methods used include manual delineation of enhanced regions, which is time-consuming particularly for large volume databases [6] and region growing for high CT number (HCTN) object segmentation where the largest objects are assumed to be bone [16]. Alternatively, bone can be identified and removed from the contrast-enhanced CT images using one of three methods: template matching, region growing, and snake-based deformable models. The contrast-enhanced tissue of the rest of the image is separated using thresholding [19]. Region-based methods using thresholding are sensitive to noise and suffer from difficulties in choosing the optimal threshold and region connectivity [21]. Structural-based approaches such as snakes and template matching can employ the structural properties of the object to perform a

more precise segmentation; however, the accuracy of the results are highly dependent on the initial curves or structures, which can be obtained using either manual segmentation or again employing thresholding or template matching approaches [23]. Finding a suitable template is a difficult task given that images are taken from a wide area of different bodies. It should be noted that none of the aforementioned methods use fuzzy classifiers for bone and CEF segmentation.

In this study, an algorithm for segmentation and classification of irregular shapes of regions containing contrast medium usually found in clinical CT images is proposed for wider applicability of the SCC algorithm for correction of oral contrast artifacts in CTAC. The basic idea consists of finding regions with high density and classifying them as bone or oral contrast material followed by the use of an appropriate calibration curve for generation of artifact-free attenuation map. The novelty of the proposed approach is the combination of a region-based technique with a boundary-based technique, which allows more accurate segmentation of bone contours, thus leading to reduced miss-segmentation and misclassification of objects. The classification stage uses many features such as volume, mean, maximum, and recursive layer mean of objects to classify them into bone and CEF using a knowledge-based fuzzy classifier. Finally, CT numbers of pixels belonging to the segmented CEF regions are substituted with their equivalent effective bone CT numbers. The initial evaluation of our segmentation algorithm for correction of contrast agent artifacts is presented using clinical data. The algorithm is still being refined to improve its computational performance and further validated in clinical setting.

Materials and methods

Segmentation algorithm

Automated bone segmentation is a difficult task owing to the articulated structure of the vertebrae, its fine borders, and rib frangibility in CT images particularly in the presence of CEF in the abdomen [24]. Two methods were implemented: the first is based on region-based segmentation with thresholding and region growing, whereas the second uses a hybrid technique combining boundary- and region-based segmentations. Figure 1 shows a flowchart describing the different steps of the proposed algorithm. The results presented in this study use the latter technique as it proved to perform better for the task at hand.

Region-based segmentation

Region-based segmentation techniques rely on the assumption that adjacent pixels in the same region have similar visual features such as gray level, color value, or texture. There are two classes of techniques: *split and merge* and *seeded region growing* [21]. The performance of the algorithm highly depends on the selected homogeneity criterion and the seed as starting point when using the *seeded approach.* Our method utilizes a seeded region growing algorithm along with a threshold-based similarity criterion. A seed is placed on the HCTN objects, which starts to grow by combining neighboring voxels until no more voxels can be included. The connected HCTN objects can then be extracted when the seed growth stops. The thresholds used to select the seeds and regions were obtained experimentally as 400 and 300 HU, respectively. This step allows to extract HCTN objects consisting of CEFs and high-density parts of bones in the dataset. As mentioned earlier, marrow density is slightly above that of soft tissue, therefore, only the HCTN parts of bones are segmented, whereas the inner parts such as marrow will be missed out as shown in Fig. 2.

The correct segmentation of the inner parts is an important step since some features used for classification are based on the intensities of these regions. A hole filling technique is used to segment the inner parts since trabecular bone has high-density borders surrounding them. The algorithm allows to segment CEF objects and bones with lower density in the inner parts. The main drawback of the technique is that the inner parts of bones are missed given the difficulty in accurately detecting external borders (Fig. 2).

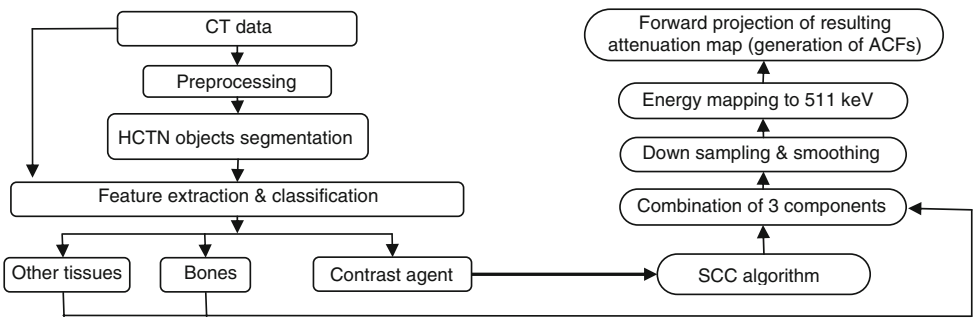

Fig. 1 Flowchart illustrating the different steps of the algorithm used for segmentation and correction of oral contrast artifacts

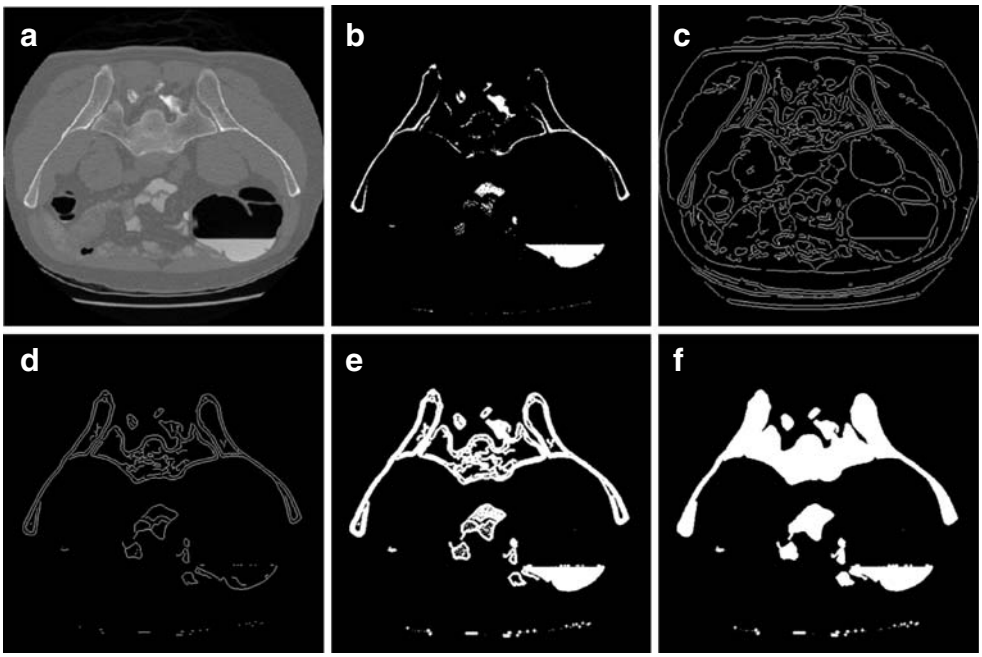

Fig. 2 Original CT image (**a**), marrow messiness by a simple threshold applying (**b**), borders detected by Canny edge operator (**c**), selected borders of Canny operator (**d**), combination of region based with borders (hybrid method; **e**), final objects after hole filling (**f**)

Hybrid segmentation

It is well known that simple segmentation methods such as thresholding and region growing are not sufficient for such complicated tasks. This is because of two main difficulties: firstly, bone marrow can not be easily segmented as bone given that its density range is similar to that of soft tissue and secondly, the linear attenuation coefficients (or CT numbers) of thin edges near the interfaces where bone and soft tissue are very close are underestimated due to partial volume averaging typically encountered in tomographic imaging [19]. The latter problem becomes more challenging with thicker slices. In this situation, boundary-based methods are highly desired as a complementary approach to achieve accurate segmentation.

Region-based segmentation techniques do not employ border properties, leading to inaccurate segmentation in many situations, which can be compensated by boundary-based methods. Boundary-based techniques rely on the assumption that pixel values change rapidly at the boundary between two regions [22]. Many edge detection techniques can be used including simple operators such as Sobel and Prewitt and Roberts or more complex ones such as the Canny edge detector [25]. It has been shown that Sobel and Prewitt edge operators produce an incomplete contour, which is not suitable for fine border extraction [22]. The Canny edge operator allows to solve this problem because of its strength to detect different directional edges or boundaries [25].

The aforementioned problems with trabecular bone segmentation can be eliminated by integrating the results of the boundary-based approach with the region-based technique. In this application, the Canny edge operator was applied as an edge detector. Trabecular bone boundaries extraction (in this case the ribs and vertebrae) is a good example to show the performance of Canny operator to detect weak edges. Two major limitations of this operator are the generation of undesired borders and unclosed boundaries (Fig. 2).

The first problem occurs owing to tissue inhomogeneity, presence of other organ borders, and noise effects. To eliminate extra borders, the seeds generated from HCTN objects leading to extraction of only those borders that are related to HCTN objects are utilized. To this end, a binary mask of HCTN objects is produced by applying a threshold to image data. The threshold level was determined experimentally to be 350 HU. Then, this mask was dilated using a traditional dilation process with a cubic square having a width of 3 pixels as a structuring element to ensure that it contains the border of HCTN objects. Finally, this mask was applied on borders obtained using Canny operator to eliminate extra borders, i.e., those that are not connected to HCTN ones. The low threshold adopted guaranties to keep all useful borders and to eliminate extra borders of soft tissue and inner body air pockets [20] as shown in Fig. 2. The second problem is unclosed boundaries and conversion of edges to regions. Although actual region boundaries are closed curves, problematic cases might produce unclosed borders where post-processing such as edge tracking, gap filling, smoothing, and thinning could be performed to obtain closed region boundaries [21]. For this purpose, small disconnectivity of borders that is possibly induced by noise or region inhomogeneity must be solved to produce closed regions.

This can be achieved by applying border dilation that can connect the gaps between up to two voxels. Gaps filling of more than two voxels may lead to unrelated adjacent border connections, which are undesired and troublesome. In addition, since we are targeting HCTN objects with high intensity, this property was used for object filling and compensation of possible gaps resulting from the use of high thresholds. Our experiments showed that a threshold of 600 HU is an adequate choice. Following hole filling of objects, a more accurate segmentation of HCTN objects was achieved [20] (Fig. 2). It might happen that large objects made by undesired connections between bone and CEF resulting from beam hardening artifacts lead to misclassification of segmented objects. To overcome this problem, a morphological object erosion approach was applied to eliminate the undesired narrow connections. It should be noted that dilation and erosion are two fundamental morphological operations widely used in image processing. Dilation adds pixels to the boundaries of objects in an image, whereas erosion removes pixels on object boundaries. In the context of our particular application, the number of pixels added or removed from the objects in an image depends on the size and shape of the structuring element used to process the image [26].

Feature extraction and classification

Pattern recognition and classification rely on the extraction and selection of features that adequately characterize the objects of interest. The task of identifying the features that perform well in a classification algorithm is a difficult issue, and the optimal choice can be non-intuitive [27, 28]. Classifiers utilize these features to classify the objects that have different types and shapes. Among available classifiers, fuzzy logic improves the classification and decision support systems by allowing the use of overlapping class definitions in addition to improving the interpretability of the results. In this study, we applied the Mamdani-type fuzzy classifier, which uses rules describing each class of customers [28, 29]. The features used for generation of fuzzy rules include volume, mean, minimum, maximum, variance, and recursive mean of outer layer's object. The recursive layer mean is one of the most important features that rely on the fact that the marrow's bone density is less than outer bone area; however, CEF has a uniform density distribution under accepted diet protocols regardless of some rare cases. This feature is computed using object's outer surface CT values after erosion using a recursive algorithm. In addition, the object's volume was used as an important feature especially in large objects. The fuzzy classifier rules are extracted based on expert knowledge in the sense that rules and membership functions are defined using results from supervised classification.

Graphic user interface (GUI)

A graphical user interface (GUI) running under Matlab 7.4.0 was developed by an easy-to-use concept for generation of the attenuation map following the SCC technique. The user is asked to choose the segmentation and classification parameters and additional parameters required for application of SCC and CTAC algorithms. According to the information provided and options selected by the user, the software loads the CT images in DICOM format, which can be viewed in any desired plane (sagittal, axial, and coronal) with the possibility of changing the color scale and contrast. Thereafter, the procedures involved including edge detection, HCTN segmentation, feature extraction, classification, SCC, and generation of the attenuation map are performed. Several measurement and viewing features such as drawing ROIs, profiles, and associated statistical estimates have been considered. An additional option was also included to allow manual handling of possible misclassification of small objects in complex cases. This can be performed by selecting the misclassified objects and changing the class assigned from bone to CEF and vice versa.

Patient studies

The assessment of CTAC accuracy in the presence of oral contrast agent was performed using 21 clinical CT colonoscopy datasets collected for the detection of colorectal neoplasia in an average-risk screening population and two clinical whole-body PET/CT examinations. The diagnostic CT datasets were used to test our segmentation and SCC algorithms during the generation of the attenuation map at 511 keV required for the CTAC procedure, whereas the PET/CT data were used to evaluate the clinical feasibility of the technique and to assess the impact of overestimating the attenuation map on the resulting PET reconstructions.

The CT data sets were obtained from the study of Pickhardt et al. [30] where the patients were recruited primarily through referral for screening colonoscopy (in asymptomatic patients). Adults between 50 and 79 years of age with an average risk of colorectal cancer (and adults 40 to 79 years of age with a family history of colorectal cancer) made up the study group. Patients underwent standard 24-h colonic preparation with the oral administration of 90 ml of sodium phosphate and 10 mg of bisacodyl. As part of their clear-liquid diet, patients also were given 500 ml of barium (2.1% by weight; Scan C, Lafayette Pharmaceuticals, Lafayette, IN, USA) for solid-stool tagging and 120 ml of diatrizoate meglumine and diatrizoate sodium (Gastrografin, Bracco Diagnostics, Princeton, NJ, USA) for the opacification of luminal fluid. The CT protocol consisted of the following procedures. On the

insertion of a small flexible rectal catheter, pneumocolon was achieved through the patient-controlled insufflation of room air immediately before scanning. CT scanning was performed in the supine and prone positions while the patient held his or her breath using the eight-slice GE LightSpeed Ultra CT scanner (GE Healthcare Technologies, Waukesha, WI, USA). The CT scanning procedure involved the use of 2.5-mm collimation, a table speed of 15 mm per second, a slice thickness of 1 mm, and scanner settings of 100 mAs and 120 kVp. The CT scanner has a 540-mm source to isocenter and 950-mm source to detector distances and uses 14,592 individual ceramic scintillator detectors ($Y_2Gd_2O_3$:Eu) with 98% absorption efficiency arranged in 16 rows of 1.25-mm thickness at isocenter (8× 2.5-mm slice when using all 16 rows), each containing 880 active elements and 32 reference elements.

Two PET/CT studies deemed to be problematic were referred to the Nuclear Medicine Division of Geneva University Hospital for a whole-body diagnostic PET/CT scan. The patients have had barium administration per os 2 days ago for esophageal, gastric, and duodenal transit assessment, which is known to remain in the abdomen for a few days after administration. PET/CT data acquisition was performed on a Biograph Sensation 16 (Siemens Medical Solutions, Erlangen, Germany) using a standard protocol recommended by the manufacturer. The PET module of the system consists of 39 rings with a total of 24,336 lutetium oxyorthosilicate crystals of dimensions 4×4×25 mm. The PET scanner has an axial field of view of 162 mm and operates in fully 3-dimensional (3D) mode. The CT module of the system consists of a 16-row ceramic detector with 1,344 channels per row and adaptive collimation. The PET acquisition was started approximately 60 min after injection of 370 MBq of [^{18}F]FDG. The PET emission study (3 min per bed position) followed immediately the CT study used for attenuation correction. The latter procedure was performed under standard conditions (120 kVp, 180 mAs, 16×1.5 collimation, a pitch of 1.2, and 1 s per rotation).

Attenuation correction and image reconstruction

The CT-based attenuation maps at 511 keV derived from the clinical colonoscopy CT data sets were generated as follows. The CT images were first down-sampled to 128× 128 followed by Gaussian smoothing to match the spatial resolution of the PET scanner. The CT numbers were then transformed to linear attenuation coefficients at 511 keV using the calculated bi-linear calibration curve based on the method proposed by Bai et al. [31]. The calibration curve for the LightSpeed Ultra CT scanner at 120 kVp and 100 mAs was computed using a cylindrical polyethylene phantom containing 16 cylindrical holes filled with a mixed solution of K_2HPO_4 and water with concentrations varying between 50 and 1,800 mg/cm^3 to simulate cortical bone with different densities [32].

For the PET/CT data set, the CT images required for creation of CT-based attenuation maps were transferred through the hospital network to another computer for offline processing. The images were then corrected for the presence of contrast medium using the segmentation algorithm described below and then imported back to the PET/CT console and used for attenuation correction of the PET data. In the CTAC procedure, the attenuation coefficients of contrast agent materials have to be converted from the effective CT energy (75 keV at 120-kVp tube voltage for this scanner) to 511 keV. However, currently available energy-mapping algorithms are based on the assumption that image contrast in the CT data is contributed by mixtures of air, soft tissue, and bone. The presence of contrast medium complicates this process since two regions that have the same CT number may indeed have different chemical compositions, for example bone/soft tissue and contrast agent/soft tissue. As a result, the region containing contrast medium can be misclassified as high-density bone and will be assigned an incorrect scaling factor. This issue can be worked out using the SCC algorithm as follows. First, the regions containing contrast medium are segmented and second, the CT number in each pixel within the segmented region is substituted with the corresponding effective bone CT number to create the corrected attenuation map [6]. It should be noted that the effective bone CT number is the value that produces the correct linear attenuation coefficient for the contrast agent when converted from CT energy to PET energy. Using the bi-linear calibration curve energy-mapping algorithm, it is computed as [6]:

$$\mathrm{CT}_{\mathrm{eff}} = \mathrm{CT}_{\mathrm{Bone}} \left(\frac{\mu_{\mathrm{CA}}^{\mathrm{PET}} - \mu_{\mathrm{Water}}^{\mathrm{PET}}}{\mu_{\mathrm{CA}}^{\mathrm{CT}} - \mu_{\mathrm{Water}}^{\mathrm{CT}}} \right) \times \left(\frac{\mu_{\mathrm{Bone}}^{\mathrm{CT}} - \mu_{\mathrm{Water}}^{\mathrm{CT}}}{\mu_{\mathrm{Bone}}^{\mathrm{PET}} - \mu_{\mathrm{Water}}^{\mathrm{PET}}} \right) \quad (1)$$

Where $\mu_{\mathrm{CA}}^{\mathrm{PET}}, \mu_{\mathrm{Water}}^{\mathrm{PET}}, \mu_{\mathrm{Bone}}^{\mathrm{PET}}, \mu_{\mathrm{CA}}^{\mathrm{CT}}, \mu_{\mathrm{Water}}^{\mathrm{CT}}, \mu_{\mathrm{Bone}}^{\mathrm{CT}}$ are the linear attenuation coefficient for contrast agent, water, and bone at the corresponding equivalent PET and CT (75 keV) energies.

The 3D PET sinograms were corrected for detector sensitivity, dead time, scatter [33] and attenuation, and converted to 2D sinograms using Fourier rebinning [34]. PET images were then reconstructed using both uncorrected and corrected CT data sets by means of attenuation-weighted, ordered subset-expectation maximization iterative reconstruction algorithm [35]. The default parameters used in clinical routine were used for reconstruction (four iterations and eight subsets followed by a post-processing Gaussian kernel with a FWHM of 5 mm).

Assessment strategy

The figures of merit used for comparative assessment of the developed algorithms include the sensitivity of segmentation algorithms and performance evaluation of the whole segmentation and classification process. For sensitivity analysis, manual segmentation performed by an experienced radiologist was used as gold standard. The sensitivity of the segmentation algorithm is calculated as the ratio of HCTN objects estimated by the automated segmentation algorithm to manually segmented HCTN objects. The overall performance is calculated as the ratio of automatically segmented CEF objects to manually segmented CEF objects where the latter procedure was performed by an experienced radiologist and considered as the gold standard in this study. The overall error is calculated as the percentage of bone objects that were misclassified as CEF.

Results

The 21 colonoscopy CT datasets segmented using both region-based and hybrid segmentation techniques were compared in terms of accurate classification of bone and CEFs objects. Tables 1 and 2 summarize the results of the segmentation and classification algorithms using sensitivity and performance measures as figures of merit. Table 1 shows the comparative assessment of the sensitivity of segmentation algorithms using the ratio of HCTN segmented objects obtained using the proposed method to the manually segmented HCTN objects performed by an experienced radiologist as gold standard. The average sensitivity of region growing and hybrid segmentation algorithms for the 21 patients studied is 87.5% and 93.3% for CEF and 39.3% and 98.8% for bone, respectively. These results suggest that the hybrid method is able to accurately segment CEF and bone objects, whereas a major limitation of the region growing algorithm is its lower sensitivity for bone segmentation.

Table 2 shows the overall performance of the segmentation and classification algorithms, calculated as the ratio of correctly segmented and classified objects to manually segmented and classified objects. The overall average performance of the hybrid and region growing methods for CEF segmentation and classification is 90.6% and 86.1%, respectively. Likewise, the mean value of false positives (FPs), i.e., bones segmented and classified as CEF, is 0.9% for the hybrid method, which is considerably lower than for the region growing method (16.2%).

Table 3 summarizes the results of segmentation, classification, and application of the SCC algorithm on the colonoscopy CT datasets. The parameters shown include the number of detected CEF 3D objects and their total volume, the average and sum of linear attenuation coefficients at 511 keV in the classified areas, as well as the mean CT number in the regions containing CEF before and after correcting the CT data using the SCC algorithm. The relative average overestimation of linear attenuation coefficients in the same regions is also shown.

Table 1 Evaluation of region growing and hybrid segmentation methods using the sensitivity of CEF and bone segmentation as figure of merit

Patient ID	Method			
	Region growing method		Hybrid method	
	CEF segmentation sensitivity (%)	Bone segmentation sensitivity (%)	CEF segmentation sensitivity (%)	Bone segmentation sensitivity (%)
1	88.9	31.9	97.5	99.1
2	86.9	27.2	99.4	99.8
3	98.7	17.2	99.2	99.7
4	98.8	19.3	86.1	99.3
5	82.0	51.8	99.4	99.0
6	97.4	40.3	90.0	98.9
7	83.7	37.5	91.0	98.2
8	97.7	50.7	97.6	98.2
9	95.4	73.4	99.5	98.4
10	94.0	37.6	99.3	99.1
11	97.3	12.5	99.0	98.6
12	89.6	55.8	96.9	98.9
13	88.3	27.8	88.0	97.7
14	90.8	79.8	99.2	99.1
15	94.0	39.6	98.9	98.6
16	98.4	13.7	95.8	99.3
17	99.2	29.9	96.7	97.5
18	98.8	35.7	97.8	99.3
19	98.6	41.4	93.3	99.4
20	28.9	53.0	69.4	98.4
21	29.7	48.2	66.0	99.0
Average ± SD	87.5±20	39.3±17.8	93.3±9.4	98.8±0.6

Figures 3–4 illustrate representative results of the segmentation, classification, and correction of the attenuation maps on typical CT colonoscopy data. The visual assessment of segmented regions performed by an experienced radiologist confirmed the accuracy of the algorithm for delineation of contrast-enhanced regions. Although some misclassification of small areas occurred in few cases, our assessment revealed that they are too small to have a sensitive impact on the calculated attenuation correction factors (ACFs) generated by forward projection of μmaps. An alternative is to perform the fine tuning through manual correction using the developed GUI (see Fig. 4b). In Figs. 3–4b, the regions containing contrast medium are labeled with green color, whereas the bony regions are labeled with red color. Figures 3–4c–d show the

Table 2 Overall performance evaluation (segmentation and classification) of the 2 segmentation techniques

Patient ID	Method			
	Region growing		Hybrid	
	Overall CEF segmentation and classification performance (%)	Overall relative error (segmented bone classified as CEF)	Overall CEF segmentation and classification performance (%)	Overall relative error (segmented bone classified as CEF)
1	88.6	11.9	96.9	1.4
2	85.0	7.6	95.5	0.9
3	98.1	20.8	98.0	0.2
4	98.5	40.2	85.5	2.7
5	81.0	27.9	97.6	1.5
6	94.5	27.2	84.5	0.8
7	82.2	22.2	88.1	2.0
8	94.6	14.0	91.5	1.5
9	91.0	7.3	91.0	0.4
10	93.1	5.6	97.6	0.2
11	96.2	20.0	96.9	0.2
12	88.0	3.3	93.6	0.7
13	87.5	12.8	86.4	0.5
14	90.5	2.7	98.6	0.9
15	93.8	6.3	98.5	0.2
16	98.1	6.8	95.2	0.1
17	98.2	12.4	94.7	0.4
18	94.1	31.0	88.8	3.7
19	97.8	43.4	91.9	1.0
20	28.0	8.7	67.5	0.2
21	28.7	8.6	64.0	0.2
Average ±SDD	86.1±19.9	16.2±11.9	90.6±9.4	0.9±0.9

extracted bone and contrast agent objects, whereas Figs. 3–4e–f show the μmap generated from CT images before and after applying the SCC algorithm. The overestimation of attenuation coefficients in the regions containing contrast medium is obvious on the original μmaps (Figs. 3–4e). Figures 3–4g show a horizontal profile through the μmaps shown in Figs. 3–4e–f to better illustrate the difference between attenuation coefficients in the generated μmaps before and after correction.

The clinical PET/CT studies known to be problematic (esophageal, gastric, and duodenal transit assessment using barium) demonstrate the applicability of the technique in clinical setting even in extreme cases (Fig. 5). Similarly, the overestimation of calculated μmap and activity concentration in the corresponding PET images are due to the presence of high-density contrast agent in the CT images. The original attenuation-corrected PET images were judged not adequate for interpretation by the nuclear medicine physicians. The uncorrected images confirmed the absence of abnormal uptake in the abdomen. The SCC PET images improved the quality of the PET scans, thus offering the possibility of quantitative analysis (standardized uptake value [SUV]), which was impossible otherwise. The artifactual high uptake in the abdomen disappeared after correcting the attenuation maps for oral contrast artifacts, which allowed to improve both the readability and interpretation of the PET scan and showed substantial decrease of the average SUV (104.3%) after correction.

Discussion

Although CT-based attenuation correction on combined PET/CT scanners has many advantages compared to conventional transmission-based attenuation correction such as the decrease in overall scanning time and increased accuracy in lesion localization in addition to generation of an almost noise-free attenuation map, it still has many limitations that need to be solved through research. In particular, the administration of oral contrast for diagnostic quality CT might result in significant bias in the generated μmaps in the regions containing high concentrations of contrast medium [14]. Our results confirm the propagation of the bias from the attenuation map into attenuation-corrected PET images.

Different strategies have been proposed for correction of contrast-related artifact in CTAC [6, 16–18, 36]. In this respect, the SCC algorithm originally proposed by Nehmeh et al. [6] proved to be efficient and easy to use. One of the drawbacks is that its application is limited to simple geometrical shapes reflecting the spatial distribution of contrast medium in the body [6, 7]. One of the main challenges in the practical implementation of the algorithm in clinical setting is the segmentation and classification of regions containing contrast media. In this study, we developed an automated segmentation algorithm for classification of regions containing oral contrast medium to enable correction for artifacts during the CTAC procedure. The application of the SCC algorithm to clinical data showed that the algorithm is efficient provided that accurate segmentation and classification of regions containing high concentration of contrast agent can be achieved.

The visual assessment by an experienced radiologist confirmed the accuracy of CEF segmentation and classification when using the hybrid segmentation method. The technique allows to reduce the unfavorable effects of CEF during PET reconstruction. The overall average performance of the hybrid method for CEF segmentation and classification (90.6%) provides evidence of the applicability of the method in clinical setting. On the other hand, the percentage of objects falsely recognized as CEF (0.9%) is a proof of the robustness of the method. The lower performance of the region growing method (86.1%) and

Table 3 Comparison of the sum of attenuation coefficients and mean attenuation coefficient at 511 keV of the generated μmaps and the mean CT number of the regions concentrating contrast agent before and after application of the SCC algorithm using the hybrid technique as segmentation method. The total number of CEF objects and voxels following dow-sampling are are also shown

Patient ID	No. of manually segmented CEF objects	Total no. of CEF voxels after down-sampling	$\sum\mu_{511\ keV}$/mean $\mu_{511\ keV}$/mean CT number in CEF objects before SCC	$\sum\mu_{511\ keV}$/mean $\mu_{511\ keV}$/mean CT number in CEF objects after SCC	Relative overestimation of mean $\mu_{511\ keV}$ (%)
1	55	79,396	2,182.8/0.123/528.6	172.0/0.098/41.7	25.8
2	76	124,019	3,439.0/0.128/609.4	271.0/0.098/48.0	29.6
3	64	62,500	1,388.4/0.132/698.7	109.4/0.099/55.1	33.9
4	79	51,936	1,847.6/0.132/684.0	145.6/0.099/53.9	33.2
5	89	26,576	908.8/0.130/657.5	71.6/0.099/51.8	31.9
6	66	68,464	2,752.1/0.136/772.9	216.9/0.099/60.9	37.3
7	76	30,226	949.7/0.127/604.1	74.8/0.098/47.6	29.4
8	88	37,418	1,116.8/0.126/573.9	88.0/0.098/47.6	28.0
9	76	53,282	1,773.6/0.129/640.0	139.8/0.099/50.4	31.1
10	154	142,774	4,096.6/0.125/551.7	322.9/0.098/43.5	26.9
11	75	45,863	1,433.6/0.127/601.0	113.0/0.098/47.4	29.2
12	117	84,227	3,255.7/0.135/743.2	256.6/0.099/58.6	36.0
13	97	112,814	3,854.7/0.130/657.0	303.8/0.099/51.8	31.9
14	130	133,018	3,881.0/0.125/561.0	305.9/0.098/44.2	27.3
15	250	137,595	4,592.1/0.129/641.7	361.9/0.099/50.6	31.2
16	120	184,271	2,389.7/0.122/498.7	188.3/0.098/39.3	24.4
17	105	63,502	2,081.4/0.129/630.2	164.0/0.099/46.7	30.6
18	89	29,538	1,026.1/0.131/667.9	80.9/0.099/52.6	32.4
19	67	64,432	1,899.8/0.125/566.9	149.7/0.098/44.7	27.6
20	93	71,629	1,008.8/0.131/661.5	72.6/0.099/53.8	32.8
21	73	66,284	2,752.1/0.136/772.9	216.9/0.099/60.9	37.3
Average ± SD	97.1±42.6	79,513±43,323	2,315±1,156/0.128±.0039/634±75	182±91/.098±.0005/50±6	30.8±3.5

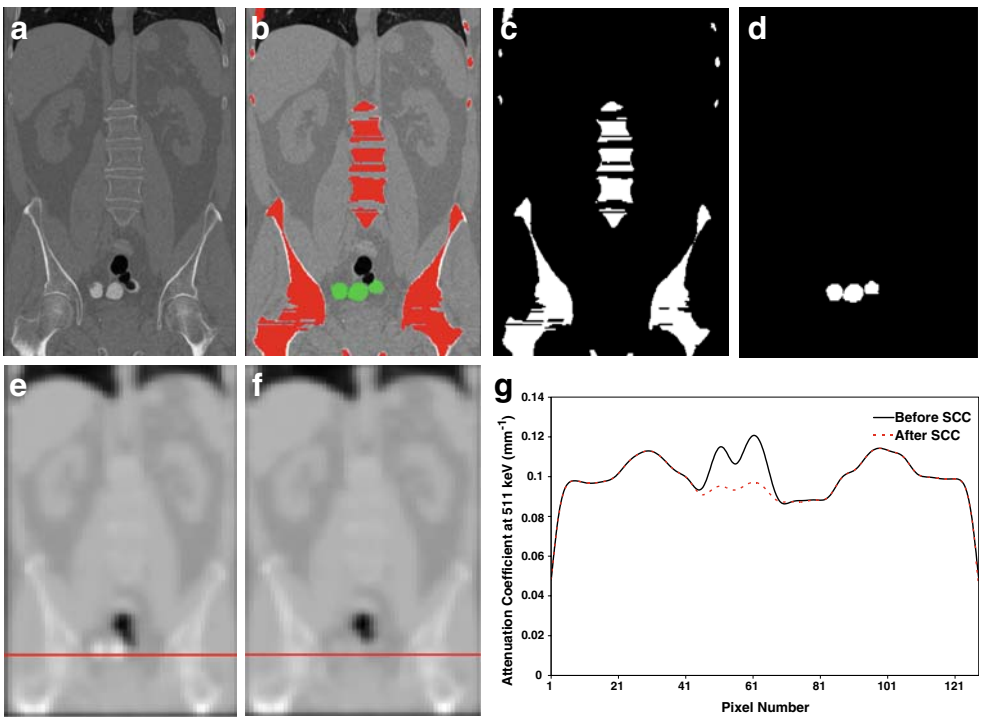

Fig. 3 Original contrast-enhanced CT image (**a**), segmented CT image (**b**), bone objects (**c**), contrast agent objects (**d**), generated μmap from original CT (**e**), and generated μmap after SCC (**f**). Horizontal profiles (position shown in **e**–**f**) through the generated attenuation maps before and after applying SCC (**g**)

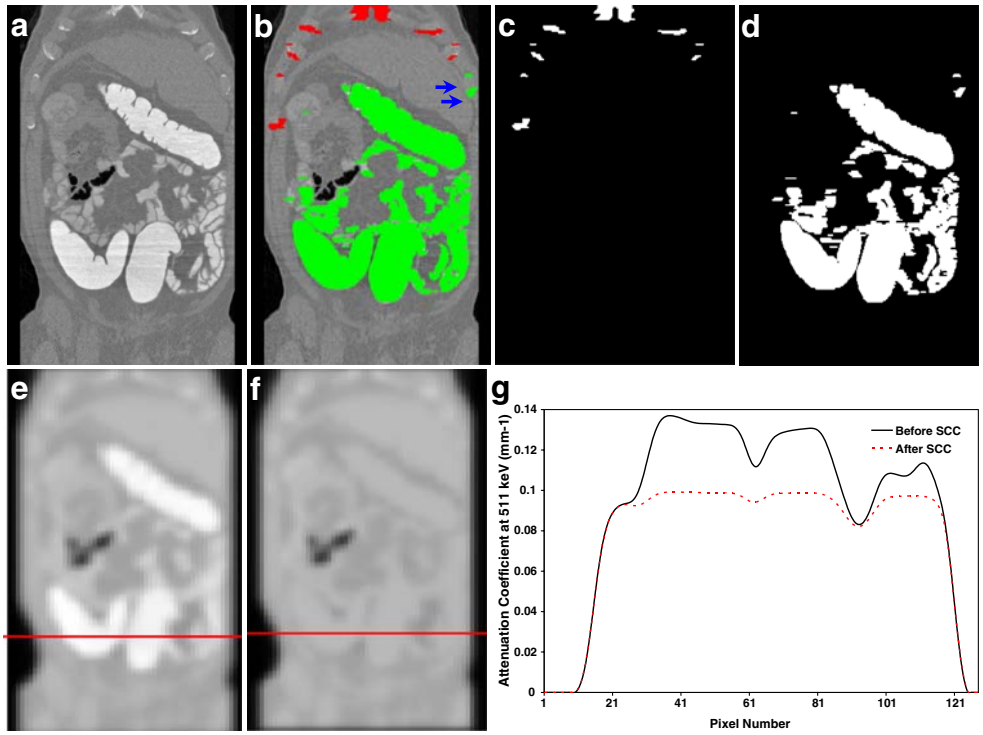

Fig. 4 Original contrast-enhanced CT image (**a**), segmented CT image (**b**), bone objects (**c**), contrast agent objects (**d**), generated μmap from original CT (**e**), and generated μmap after SCC (**f**). Horizontal profiles (position shown in **e**–**f**) through the generated attenuation maps before and after applying SCC (**g**). The *arrows* in **b** show the small miss-classified area that can be corrected manually using the developed GUI following visual assessment

the higher number of miss-segmented objects (16.2%) is an evident indication of the limitations of the technique. The main source of FPs (i.e., regions falsely classified as a CEF) backs to incomplete bone segmentation (segmentation of bone outer parts only), which is the main drawback of region-based segmentation accountable for yielding incorrect feature extraction and thus wrong classification. The high rate of FPs clearly confirms this statement. Other possible causes of FP are artifacts resulting from beam hardening and field-of-view truncation.

The main source of FNs, i.e., CEF regions falsely not classified as a CEF, backs to incomplete feature extraction especially in small CEF regions (Fig. 4). Small CEF objects might become too small after smoothing and downsampling. Manual correction through user interaction allows to change the class assigned to misclassified objects.

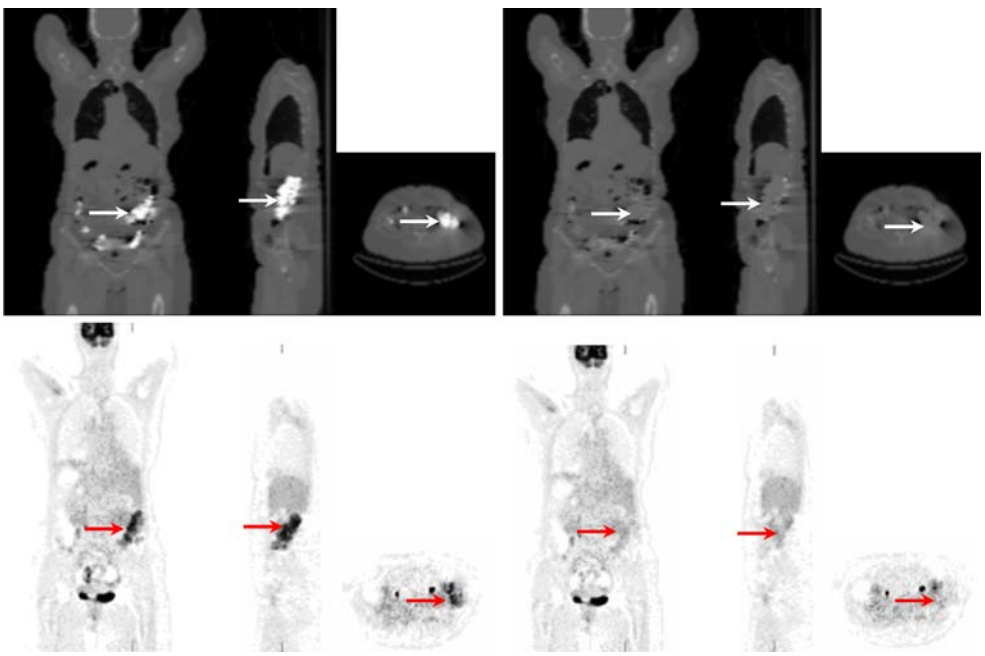

Fig. 5 Illustration of generated μmap (*top row*) and CT-attenuation-corrected PET images (*bottom row*) in different views before (**a**) and after (**b**) correction of oral contrast artifacts (*arrows*). Note that the artifactual high uptake in the abdomen disappeared after correcting the attenuation maps for oral contrast artifacts, which allowed to improve the readability and interpretation of the PET scan

Another source of error for CEF miss-segmentation is the non-optimal selection of the threshold used. Choosing a lower threshold (~350 HU) will undoubtedly increase the number of segmented voxels containing low-contrast concentration.

The region growing algorithm makes use of the assumption that the skeleton in the examined region is connected and isolated from CEF, which renders the results very sensitive to the selected seed. However, in real case studies, small overlaps or contacts between bone and CEF are fairly common and often unpredictable for a large image volume, which leads to wrong classification of some regions. In contrast, the hybrid method enables complete segmentation of the bony structures, thus allowing more accurate feature extraction and classification irrespective of the selected seed. The proposed hybrid segmentation method occasionally fails to correctly segment CEF regions when they are too close to the bone. This failure becomes more important when large volume objects made by an undesired connection between bone and CEF lead to a complex object consisting of a mixture of bone and CEF. To overcome this problem, a morphological object erosion approach was applied to eliminate the undesired narrow connections.

Qualitative visual assessment also showed that the proposed hybrid segmentation algorithm has the ability to effectively segment the CT images of several patients even though the images contained a large amount of anatomical variability and different oral contrast diet. However, miss-segmentation and misclassification for small objects were found in a few cases, thus causing small errors in the final result. Although the developed segmentation algorithm seems to be applicable in a clinical environment, it still has some limitations for the detection of regions with CT numbers lower than 350 HU. This makes the algorithm useless in PET/CT centers using low-concentration contrast agents (solutions of 2% barium). The use of low-concentration contrast agents allows to minimize the impact of contrast agent artifacts during the CTAC procedure at the expense of decreasing the diagnostic quality of clinical CT images.

It must be noted that the Mamdani classifier used in this study is based on expert knowledge and rules, which influence to a great extent the final result. Other classifiers will be investigated to improve the accuracy of the classification process. In addition, since large volume objects may consist of a mixture of CEF and bone, more elaborate algorithms such as the distance transform map that allows to eliminate wrong object connections could be used. Likewise, more accurate handling of external contours using more sophisticated edge detection operators combined with more precise contour to region conversion utilities would be an asset.

Conclusion

In this study, we developed an automated segmentation algorithm for classification of irregular shapes of regions containing contrast medium usually found in clinical CT images for wider applicability of the SCC algorithm to correct for oral contrast artifacts in CTAC. The proposed hybrid method allows to achieve complete segmentation of bone and CEF leading to correct objects classification, whereas region growing leads to incomplete bone segmentation where small bones are classified as CEF. The visual assessment of segmented regions using clinical CT images performed by an experienced radiologist confirmed the accuracy of the hybrid segmentation and classification algorithm for delineation of contrast-enhanced regions. The quantitative analysis of generated μmaps from clinical CT colonoscopy datasets revealed a substantial overestimation of attenuation coefficients in the 3D regions classified as contrast agent depending on concentration and volume. Two clinical PET/CT studies known to be problematic demonstrated the applicability of the technique in clinical setting. More importantly, correction of oral contrast artifacts improved the readability and interpretation of the PET scan and showed substantial decrease of the SUV after correction. The algorithm is being further refined by speeding up the segmentation and classification process and further validated in clinical setting by processing a large pool of patient datasets.

Acknowledgments The authors would like to thank Drs. Nehmeh Sadek, Arman Rahmim, and Perry J. Pickhardt for their valuable support and for providing part of the clinical datasets used in this work. This work was supported by the Research Center for Science and Technology in Medicine, Medical Sciences/University of Tehran, Iran and the 12th Razi International Festival in Medical Sciences. HZ acknowledges the support of the Swiss National Science Foundation under grant No. 3152A0-102143.

References

1. Townsend DW, Carney JPJ, Yap JT, Hall NC. PET/CT today and tomorrow. J Nucl Med. 2004;45:4S–14.
2. Dizendorf E, Hany TF, Buck A, von Schulthess GK, Burger C. Cause and magnitude of the error induced by oral CT contrast agent in CT-based attenuation correction of PET emission studies. J Nucl Med. 2003;44:732–8.
3. Groves AM, Kayani I, Dickson JC, Townsend C, Croasdale I, Syed R, et al. Oral contrast medium in PET/CT: should you or shouldn't you? Eur J Nucl Med Mol Imaging. 2005;32:1160–6.
4. Tateishi U, Maeda T, Morimoto T, Miyake M, Arai Y, Kim E. Non-enhanced CT versus contrast-enhanced CT in integrated PET/CT studies for nodal staging of rectal cancer. Eur J Nuc Med Mol Imaging. 2007;34:1627–34.
5. Mainenti P, Salvatore B, D'Antonio D, De Falco T, De Palma G, D Armiento F, et al. PET/CT colonography in patients with colorectal polyps: a feasibility study. Eur J Nuc Med Mol Imaging. 2007;34:1594–603.

6. Nehmeh SA, Erdi YE, Kalaigian H, Kolbert KS, Pan T, Yeung H, et al. Correction for oral contrast artifacts in CT attenuation-corrected PET images obtained by combined PET/CT. J Nucl Med. 2003;44:1940–4.
7. Ay MR, Zaidi H. Assessment of errors caused by x-ray scatter and use of contrast medium when using CT-based attenuation correction in PET. Eur J Nucl Med Mol Imaging. 2006;33:1301–13.
8. Antoch G, Freudenberg LS, Beyer T, Bockisch A, Debatin JF. To enhance or not to enhance? 18F-FDG and CT contrast agents in dual-modality 18F-FDG PET/CT. J Nucl Med. 2004;45(Suppl 1):56S–65S.
9. Antoch G, Kuehl H, Kanja J, Lauenstein TC, Schneemann H, Hauth E, et al. Dual-modality PET/CT scanning with negative oral contrast agent to avoid artifacts: introduction and evaluation. Radiology. 2004;230:879–85.
10. Dizendorf EV, Treyer V, Von Schulthess GK, Hany TF. Application of oral contrast media in coregistered positron emission tomography-CT. AJR Am J Roentgenol. 2002; 179:477–81.
11. Yau Y-Y, Chan W-S, Tam Y-M, Vernon P, Wong S, Coel M, et al. Application of intravenous contrast in PET/CT: does it really introduce significant attenuation correction error? J Nucl Med. 2005;46:283–91.
12. Berthelsen AK, Holm S, Loft A, Klausen TL, Andersen F, Hojgaard L. PET/CT with intravenous contrast can be used for PET attenuation correction in cancer patients. Eur J Nucl Med Mol Imaging. 2005;32:1167–75.
13. Nakamoto Y, Chin BB, Kraitchman DL, Lawler LP, Marshall LT, Wahl RL. Effects of nonionic intravenous contrast agents at PET/CT imaging: phantom and canine studies. Radiology. 2003; 227:817–24.
14. Zaidi H, Montandon M, Alavi A. Advances in attenuation correction techniques in PET. PET Clin 2007;2:191–217.
15. Kinahan PE, Hasegawa BH, Beyer T. X-ray-based attenuation correction for positron emission tomography/computed tomography scanners. Semin Nucl Med. 2003;33:166–79.
16. Carney J, Beyer T, Brasse D, Yap JT, Townsend DW. CT-based attenuation correction for PET/CT scanners in the presence of contrast agent. Nuclear Science Symposium Conference Record, 2002 IEEE 2002;3:1443–6.
17. Buther F, Stegger L, Dawood M, Range F, Schafers M, Fischbach R, et al. Effective methods to correct contrast agent-induced errors in PET quantification in cardiac PET/CT. J Nucl Med. 2007; 48:1060–8.
18. Kinahan PE, Alessio AM, Fessler JA. Dual energy CT attenuation correction methods for quantitative assessment of response to cancer therapy with PET/CT imaging. Technol Cancer Res Treat. 2006;5:319–27.
19. Yao J, O'Connor SD, Summers R. Computer aided lytic bone metastasis detection using regular CT images. Proceedings of SPIE, Medical Imaging 2006: Image Processing, San Diego, CA 2006;6144:1692–700.
20. Bidgoli J, Ahmadian A, Akhlaghpor S, Alam N, Mahmodabadi S. An efficient colon segmentation method for oral contrast-enhanced CT colonography. Conf Proc IEEE Eng Med Biol Soc. 2005;4:3429–32.
21. Fan J, Yau DKY, Elmagarmid AK, Aref WG. Automatic image segmentation by integrating color-edge extraction and seeded region growing. IEEE Trans Image Process. 2001;10:1454–66.
22. Palmer PL, Dabis H, Kittler J. A performance measure of boundary detection algorithms. Comput Vis Image Und. 1996; 63:476–94.
23. Xu C, Prince JL. Snakes, shapes, and gradient vector flow. IEEE Trans Image Processing. 1998;7:359–69.
24. Ghebreab S, Smeulders AWM. Combining strings and necklaces for interactive three-dimensional segmentation of spinal images using an Integral deformable spine model. IEEE Trans Biomed Eng. 2004;51:1821–9.
25. Canny JF. A computational approach to edge detection. IEEE Trans Pattern Anal Machine Intell. 1986;8:679–98.
26. Soille P. Morphological image analysis: principles and applications. New York: Springer; 1999.
27. de Oliveira JV. Semantic constraints for membership function optimization. IEEE Trans Systems Man and Cybernetics, Part A. 1999;29:128–38.
28. Jang JSR, Sun C, Mizutani E. Neuro-fuzzy and soft computing: a computational approach to learning and machine intelligence. Upper Saddle River: Prentice Hall; 1997.
29. Ying H, Ding Y, Li S, Shao SSA-S. Comparison of necessary conditions for typical Takagi-Sugeno and Mamdani fuzzy systems as universal approximators. IEEE Trans Systems Man and Cybernetics, Part A. 1999;29:508–14.
30. Pickhardt PJ, Choi JR, Hwang I, Butler JA, Puckett ML, Hildebrandt HA, et al. Computed tomographic virtual colonoscopy to screen for colorectal neoplasia in asymptomatic adults. N Engl J Med. 2003;349:2191–200.
31. Bai C, Shao L, Da Silva AJ, Zhao Z. A generalized model for the conversion from CT numbers to linear attenuation coefficients. IEEE Trans Nucl Sci. 2003;50:1510–5.
32. Ay MR, Zaidi H. Computed tomography-based attenuation correction in neurological positron emission tomography: evaluation of the effect of x-ray tube voltage on quantitative analysis. Nucl Med Commun. 2006;27:339–46.
33. Watson CC. New, faster, image-based scatter correction for 3D PET. IEEE Trans Nucl Sci 2000;47:1587–94.
34. Defrise M, Kinahan PE, Townsend DW, Michel C, Sibomana M, Newport DF. Exact and approximate rebinning algorithms for 3-D PET data. IEEE Trans Med Imaging. 1997;16:145–58.
35. Michel C, Sibomana M, Boi A, Bernard X, Lonneux M, Defrise M, et al. Preserving Poisson characteristics of PET data with weighted OSEM reconstruction. Conf Rec of IEEE Nuclear Science Symposium and Medical Imaging Conference, Toronto, ON, 8–14 November, 1998. 1998;2:1323–9.
36. Tang HR, Brown JK, Da Silva AJ, Matthay KK, Price DC, Huberty JP, et al. Implementation of a combined X-ray CT-scintillation camera imaging system for localizing and measuring radionuclide uptake: experiments in phantoms and patients. IEEE Trans Nucl Sci. 1999;46:551–7.